OPEN

npg

ORIGINAL ARTICLE

A single Eu²⁺-activated high-color-rendering oxychloride white-light phosphor for white-light-emitting diodes

Peng-Peng Dai[1], Cong Li[1], Xin-Tong Zhang[1], Jun Xu[2], Xi Chen[1], Xiu-Li Wang[3], Yan Jia[1], Xiaojun Wang[1,4] and Yi-Chun Liu[1]

Single-phased, high-color-rendering index (CRI) white-light phosphors are emerging as potential phosphor-converted white-light-emitting diodes (WLEDs) and as an alternative to blends of tricolor phosphors. However, it is a challenge to create a high CRI white light from a single-doped activator. Here, we present a high CRI (Ra = 91) white-light phosphor, $Sr_5(PO_4)_{3-x}(BO_3)_xCl:Eu^{2+}$, composed of $Sr_5(PO_4)_3Cl$ as the beginning member and $Sr_5(BO_3)_3Cl$ as the end member. This work utilized the solid-solution method, and tunable Eu^{2+} emission was achieved. Color-tunable Eu^{2+} emissions in response to structural variation were observed in $Sr_5(PO_4)_{3-x}(BO_3)_xCl$ solid solutions. This was further confirmed using X-ray Rietveld refinement, electron paramagnetic resonance spectroscopy, and in the photoluminescence spectra. The color-tunable emissions included the white light that originated from the combination of the blue emission of $Sr_5(PO_4)_3Cl:Eu^{2+}$ and an induced Eu^{2+} yellow emission at approximately 550 nm in the solid solution. Importantly, the white-light phosphors showed a greater R9 = 90.2 under excitation at 365 nm. This result has rarely been reported in the literature and is greater than that of (R9 = 14.3) commercial $Y_3Al_5O_{12}:Ce^{3+}$-based WLEDs. These findings demonstrate the great potential of $Sr_5(PO_4)_{3-x}(BO_3)_xCl:0.04Eu^{2+}$ as a white-light phosphor for near-UV phosphor-converted WLEDs. These results also provide a shortcut for developing a high CRI white-light phosphor from a single Eu^{2+}-doped compound.

INTRODUCTION

White-light-emitting diodes (WLED) fabricated with near ultraviolet LED (NUVLED) and tricolor phosphors are a potential substitute for current lighting sources[1–3]. However, these types of WLED devices are rather complicated, and the color balance is difficult to control[4]. Recently, single-phased, white-light phosphors have attracted more attention because they avoid most of these problems[4]. A conventional strategy using single-phased white-light phosphors is to co-dope ion pairs based on the energy transfer principle, e.g., $Eu^{2+}\rightarrow+Mn^{2+}$, $Eu^{2+}\rightarrow Tb^{3+}/Mn^{2+}$, $Ce^{3+}\rightarrow Mn^{2+}$, and $Ce^{3+}\rightarrow Tb^{3+}/Mn^{2+}$ pairs[5–14]. In these systems, the common feature is that Mn^{2+} is the red-emitting activator. However, the weak Mn^{2+} d-d transitions usually lead to additional excitation quenching paths to reduce the quantum yield (QY) and thermal stability[15–18]. A single-doping activator-activated white-light phosphor that suppresses the energy loss related to energy transfer is highly desired for phosphor-converted WLEDs. However, it is difficult to achieve white light from a compound with a single-doped activator that must also cover the entire visible lighting range from 400 nm to 700 nm.

Solid-solution phosphors are an efficient tool with which to explore white-light phosphors activated by a single-doped activator because this phosphor has a variable composition. This variable composition can simultaneously alter multiple parameters of the host lattice and thereby induce multiple crystal field environments imposed on the emission centers. By utilizing this strategy, some novel phosphors and new luminescence phenomena have been identified, such as tunable emission color, efficient luminous output, and improved thermal/chemistry stability[19–25]. For solid-solution phosphors, the end members usually must have high crystal chemical flexibility, or the end members are nearly isotypic despite crystallizing in structures with distinct space groups. $Sr_5(PO_4)_3Cl$ is an important member of the apatite-type halophosphates $M_5(XO_4)_3Cl$ compounds (M = Ca, Sr, Ba, X = P, V, Si) that has been widely investigated for nearly five decades[8,26–29]. The compound crystallizes in a hexagonal structure with a P63/m space group, can incorporate various foreign ions, and can provide abundant crystal field environments[26–29]. $Sr_5(BO_3)_3Cl$ crystallizes in an orthorhombic structure with a C2221 space group that has stoichiometrically mimicked apatite-type compounds and has been studied for almost two decades[30]. $Sr_5(BO_3)_3Cl$ also presents a rich crystal chemistry due to the wide range of possible cationic substitution[30]. Therefore, a novel oxychloride solid solution with a solid-solution containing the two traditional $Sr_5(PO_4)_3Cl$ and $Sr_5(BO_4)_3Cl$ compounds is possible based on their crystal chemistry

[1]Center for Advanced Optoelectronic Functional Materials Research, and Key Laboratory for UV-Emitting Materials and Technology of Ministry of Education, Northeast Normal University, 5268 Renmin Street, Changchun 130024, China; [2]Department of Chemistry, University of Zurich, The X-ray Crystallography Facility and The Linden Research Group, Winterthurerstrasse, 190 CH-8057 Zurich, Switzerland; [3]School of Life Sciences, Northeast Normal University, 5268 Renmin Street, Changchun 130024, China and [4]Department of Physics, Georgia Southern University, Statesboro, GA 30460, USA
Correspondence: X Zhang, Email: xtzhang@nenu.edu.cn; X Wang, Email: xwang@georgiasouthern.edu

npg
Eu^{2+}-activated high CRI white-light phosphor
P Dai *et al*

2

similarity. $Sr_5(PO_4)_3Cl:Eu^{2+}$ is a highly efficient blue-emitting phosphor for WLEDs[8], whereas $Sr_5(BO_4)_3Cl:Eu^{2+}$ phosphor presents a broadband red emission near 615 nm[31]. Therefore, a color-tunable emission that includes white light is expected from this oxychloride solid-solution compound.

In this study, the Eu^{2+}-activated $Sr_5(PO_4)_{3-x}(BO_3)_xCl$ solid-solution phosphors comprised of $Sr_5(PO_4)Cl$ as the oxychloride beginning member and $Sr_5(BO_4)_3Cl$ as the end member were synthesized via a solid-state reaction. Their structures were investigated using powder X-ray diffraction (XRD), XRD Rietveld refinement analysis, and electron paramagnetic resonance (EPR). The optical properties of the phosphors are discussed in detail using crystal structure analysis, photoluminescence (PL) excitation (PLE), transition decays, and fluorescence microscopy images. As expected, a tunable emission including white light with a high color rendering index (CRI; Ra = 91, R9 = 90.2) was achieved from the single-Eu^{2+}-doped $Sr_5(PO_4)_{3-x}(BO_3)_xCl$ solid solution at an excitation of 365 nm. To the best of our knowledge, these are the greatest indices for white-light phosphors reported, especially for those obtained by single-Eu^{2+} doping of an oxychloride compound. This study provides a shortcut for developing a high CRI white-light phosphor from a single-Eu^{2+}-doped compound. In addition, this work promotes the development of single-phased white-light phosphors.

MATERIALS AND METHODS

Materials synthesis
The $Sr_5(PO_4)_{3-x}(BO_3)_xCl$ powders were made using solid-state reaction routes. The starting materials were $SrCl_2·6H_2O$ (99.95%), H_2BO_3 (99.99%), $SrHPO_4$ (99.95%), $SrCO_3$ (99.95%), and Eu_2O_3 (99.99%). The powder mixtures were quantitatively mixed using an agate mortar and pestle, and were subsequently sintered for 3 h at 1350 °C in a CO reducing atmosphere. The products were reground and fired again for 1 h at 1350 °C in a muffle furnace and were then ground again for further characterization.

Characterization methods
The structures of the samples were identified using a Rigaku D/max-2500 X-ray diffractometer (Rigaku Co., Japan) with Cu K_α radiation ($\lambda = 0.15406$ nm). The detector covers an angular range $10° < 2\theta < 105°$ with a counting time of 5 s per step. The Rietveld refinement used a general structure analysis system (GSAS) program[32]. The peak shapes were handled using a pseudo-Voigt function with Finger-Cox-Jephcoat asymmetry to correct for axial divergence at low angles. The crystal constants of the samples were calculated using X-ray Rietveld refinement. The room temperature PL spectra were measured with a homemade PL measurement system consisting of a 365-nm NUVLED array as the excitation source and an Ocean Optics USB 4000 plug-and-play spectrometer. The PLE spectra were analyzed using a Horiba FL-3 fluorescence spectrophotometer equipped with a 450 W Xe lamp. Fluorescence microscope PL images (TE-2000 Instruments; Nikon, Japan) of the powder particles were recorded under dark-field mode using a 365-nm UV lamp excitation. Fluorescence decay time curves were measured using an Edinburgh FLS920 spectrophotometer with an nF900 flash lamp. The EPR spectroscopy was recorded using a JES-FA200 (JEOL, Japan) EPR spectrometer. The temperature-dependent luminescence was measured under temperature control (THMS-600) in combination with a homemade PL measurement system consisting of a 365-nm NUVLED array as the excitation source and a micro-Raman spectrometer (Jobin-Yvon HR800) as the detector. A full set of 14 CRIs and the average CRI (Ra) values of the powders were measured using a homemade PL measurement system with a 365-nm UV light source (LA-410, full width at half

maximum (FWHM): 5 nm, Japan) and a band-pass filter (Asahi spectra, Japan) as well as the same miniature fiber optic spectrometer with an integrated sphere. The electroluminescent (EL) spectrum and the CRI values of the commercial WLED were also measured using the same miniature spectrometer. The quantum yield (QY) was measured using a PL quantum-yield measurement system (C9920-02, Hamamatsu Photonics).

RESULTS AND DISCUSSION
Figure 1 presents the structural differences between $Sr_5(PO_4)_3Cl$ (SPO_Cl) and $Sr_5(BO_3)_3Cl$ (SBO_Cl) and a coordinated polyhedron of anions/cations. SPO_Cl crystallizes as a hexagonal structure and has two cationic sites, referred to as Sr1 and Sr2. These sites reside in the 4f and 6h sites (Figure 1a)[8]. The coordination polyhedron of Sr1/O is composed of six O atoms, and the coordination polyhedron of Sr2/O is composed of two Cl and five O atoms. The P ions are connected with four O ions, forming the PO_4 tetrahedron structure[8]. The crystallization of SBO_Cl in the orthorhombic structure is a complex three-dimensional framework of 7-, 8-, and 9-coordinate Sr-centered polyhedral and BO_3 triangular planes (Figure 1b). There are four cationic sites, which are referred to as Sr1, Sr2, Sr3, and Sr4, that reside in the 4a, 8c, 4b, and 4b sites, respectively[30]. The B ions are surrounded by three O atoms forming a BO_3 triangular plane with O-B-O bond angles near 120°.

The calculated and experimental results as well as their differences in the XRD refinement of SPO_Cl are shown in Figure 2a. The initial structural mode was established by the standard crystallographic data of the SPO_Cl (ICSD#0993). The zero point error, scale factor, and background lattice and parameters were refined first followed by the
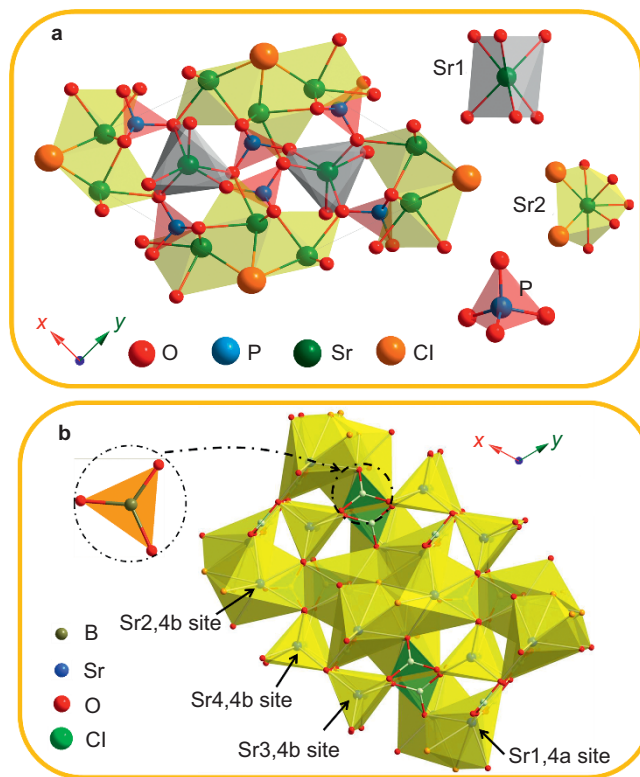

Figure 1 Crystal structures of $Sr_5(PO_4)_3Cl$ (**a**) and $Sr_5(BO_3)_3Cl$ (**b**) viewed from the *z*-direction and the coordination of the Sr/P and B/Sr sites in the end members, respectively.

profile parameters (i.e., W, V, U, X, and Y.). Finally, the structural parameters were refined. Based on the Finger-Cox-Jephcoat profile function model, the refinement of the low-angle asymmetry significantly improved the reliability of the pattern fitting. The final reliability factors for the complete pattern were $R_{wp} = 8.46\%$ and $R_p = 5.46\%$. The refined lattice parameters were a = b = 9.872(5) Å, c = 7.187(9) Å, and V = 606.7(3) Å^3. These results agree well with the results previously reported[32].

Figure 2b shows the XRD patterns of the $Sr_5(PO_4)_{3-x}(BO_3)_x$Cl:0.04Eu^{2+} (0 ⩽ x ⩽ 0.5) powders. The XRD patterns of the $Sr_5(PO_4)_{3-x}(BO_3)_x$Cl:0.04Eu^{2+} (SPBO_Cl:0.04Eu^{2+}) solid solution all maintain the characteristic pattern of the hexagonal structure of the SPO_Cl end member. These are consistent with literature values ($Sr_5(PO_4)_3$Cl, PDF card No. 16-0666)[33]. No detectable XRD peaks corresponding to impurities or other phases were observed, indicating that solid solutions were obtained. When x > 0.5, some by-products appeared in the power sample due to the large mismatch (35%) of the ionic radii of P^{5+} (r = 0.17 Å, CN = 4) and B^{3+} (r = 0.11 Å, CN = 4). We therefore believe that the $Sr_5(PO_4)_{3-x}(BO_3)_x$Cl compounds for 0 ⩽ x ⩽ 0.5 were primarily solid solutions. The XRD peaks located at 30.3° and 31.4° correspond to the (211) and (300) crystal planes, respectively. These shift slightly to the higher scattering angle with an increase in the B^{3+} ion concentrations, whereas the XRD peak at 30.7° shifts to the lower scattering angle side (Figure 2c). The XRD peaks shift toward the higher angle side. This trend is also seen on almost all of the other diffractive peaks except for the XRD peaks corresponding to the (002), (102), (222), (213), and (004) crystal planes. These observations indicate the substitution of smaller B^{3+} (r = 0.11 Å, CN = 4), for P^{5+} (r = 0.17 Å, CN = 4) changes the lattice parameters of the host. As shown in Figure 2d, the calculated lattice constants a and b decrease linearly as x increases, whereas the lattice constant c is mostly constant. The simultaneous expansion and contraction of the unit cell in different directions suggests that the anionic polyhedron substitution of PO_4 with BO_3 causes a greater distortion of the host lattice end member.

The distortion of the host lattice has a significant effect on Eu^{2+} luminescence. As reported, Eu^{2+} occupied the Sr2 sites in the SPO_Cl
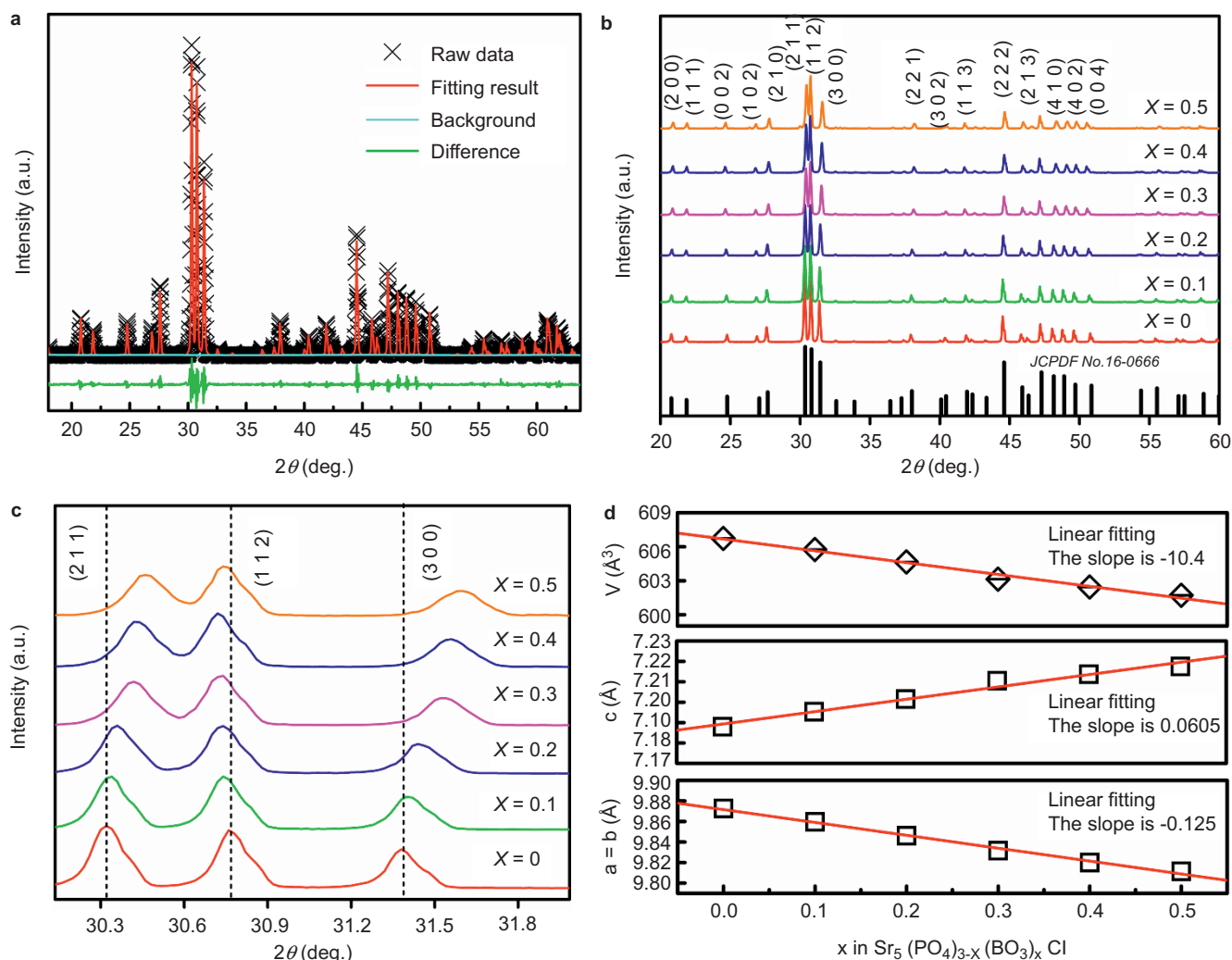

Figure 2 (a) Observed (crosses) and calculated (solid lines) XRD patterns of the Rietveld refinement of the as-prepared $Sr_5(PO_4)_3$Cl powder. (b) XRD patterns of the SPBO_Cl:0.04Eu^{2+} (0 ⩽ x ⩽ 0.5). As a reference, the standard XRD data for $Sr_5(PO_4)_3$Cl is shown. (c) Magnified XRD patterns in the region between 30° and 32° for the SPBO_Cl:0.04Eu^{2+} (0 ⩽ x ⩽ 0.5). (d) Unit cell parameters of the SPBO_Cl:0.04Eu^{2+} (0 ⩽ x ⩽ 0.5) show a contraction in the lattice parameters a and b but only a slight increase in lattice parameter c.

host lattice more often than the Sr1 sites. Therefore, only one emission band in the blue spectral region was observed[28,29]. In our case, SPO_Cl:yEu^{2+} ($0.02 \leqslant y \leqslant 0.1$) exhibited an asymmetric blue emission at approximately 446 nm under excitation at 365 nm (see Supplementary Fig. S1). As the Eu^{2+} content increased, the luminous intensity was intensified and reached a maximum at $y = 0.04$ (see Supplementary Fig. S2). Herein, we consider that most Eu^{2+} ions occupy the Sr2 sites (446 nm) rather than Sr1 sites (462 nm) in the SPO_Cl host, which supports the findings of previous reports[28,29].

Interestingly, an additional distinct emission peak at approximately 550 nm was observed under excitation at the same wavelength when doped with B^{3+} ions (see Supplementary Fig. S1). This observation suggests that the introduction of B^{3+} ions induces a distinct Eu^{2+} center that originates from the Eu^{2+} occupying a distorted crystal field environment. The emission spectra can be deconvoluted into three Gaussian components with peaks centered at approximately 446 and 462 nm (Eu(1)) and 550 nm (Eu(2)), as shown in Supplementary Fig. S1. We assign the higher-energy emission (446 and 462 nm) to Eu(1), which occupies Sr2/Sr1 sites with a weak crystal field. From the X-ray data measured here, it is difficult to determine which sites the induced Eu^{2+} ions can occupy. Therefore, we tentatively assigned the lower-energy emission (550 nm) to Eu(2) occupying the perturbed Sr2 with a strong crystal field. With an increase in the B^{3+}-doped content, the QY values of the corresponding samples obviously decrease from 82% at $x = 0$ to 53% at $x = 0.5$ at an excitation of 365 nm, which should indicate the formation of more defects in the host lattice. Optimizing the synthesis process is expected to increase the QY.

Color tunability is very significant for phosphors because it facilitates WLED color tuning[34]. The normalized PL spectra ($\lambda_{ex} = 365$ nm) of the SPBO_Cl:0.04Eu^{2+} powders ($x = 0$, 0.1, 0.2, 0.3, 0.4, and 0.5) are presented in Figure 3a. The relative intensity of the yellow to blue emission increases gradually with an increase in the B^{3+} content. This reaches a maximum at $x = 0.5$, whereas the intensity of the blue emission steadily decreases (Figure 3b). Therefore, a tunable color spectrum including white light can be obtained by combining the two emission bands located at approximately 446 and 550 nm in this SPBO_Cl:0.04Eu^{2+} solid-solution phosphors. The change in the emission ratio may be attributed to the higher number ratio of the Eu(2) relative to the Eu(1) sites. These are dependent on the structural variation in the solid-solution phosphor. Conversely, the energy transfer from the Eu(1) to Eu(2) sites also contributes to the change in the emission ratio. This will be shown and discussed in detail in the lifetime decay section.

Next, confocal fluorescence microscopy PL images were recorded using the 365-nm UV lamp excitation to demonstrate the PL characteristics of the phosphor particles. The emission color of these microcrystalline powders was visible to the naked eye and was tunable from blue to blue-greenish and ultimately to white luminescence
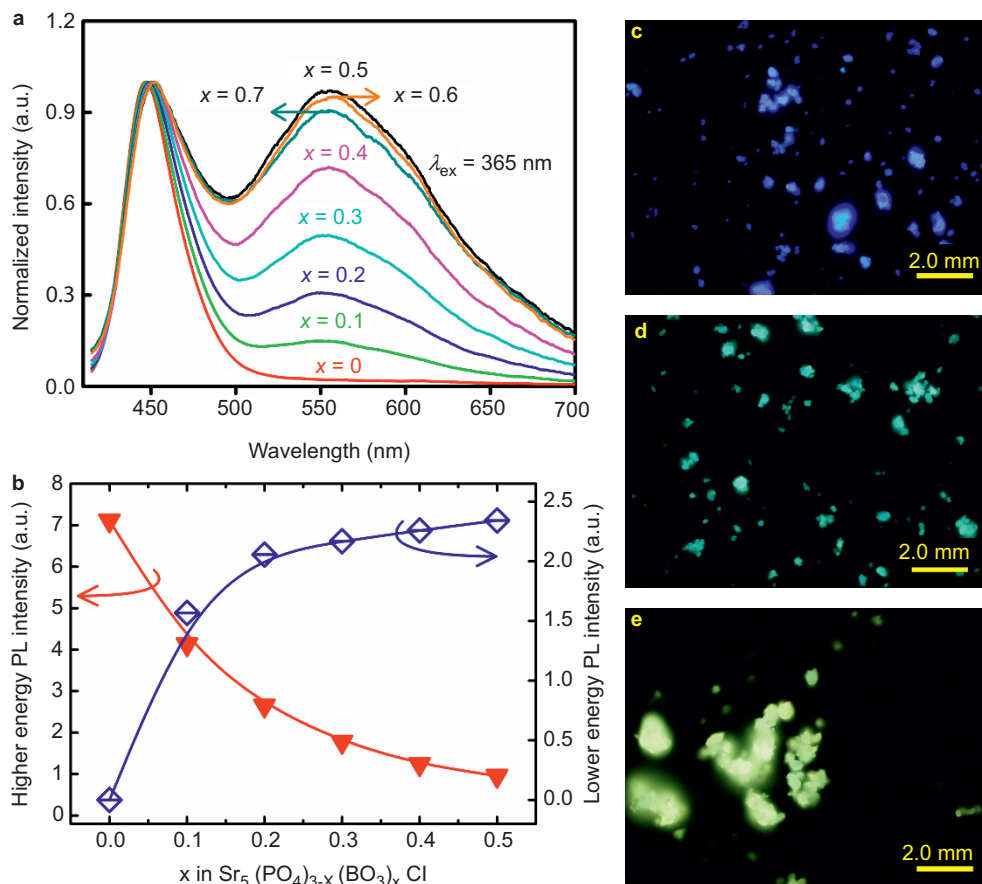

Figure 3 (**a**) Normalized PL spectra of SPBO_Cl:0.04Eu^{2+} ($0 \leqslant x \leqslant 0.5$) under excitation at 365 nm. (**b**) The integrated PL intensity of the higher-energy emission and the lower-energy emission of SPBO_Cl:0.04Eu^{2+} as a function of the B^{3+} content ($0 \leqslant x \leqslant 0.5$) under excitation at 365 nm. (**c**), (**d**), and (**e**) the fluorescence microscope PL images for SPBO_Cl:0.04Eu^{2+} ($x = 0$, 0.2, and 0.5) under excitation at 365 nm.

(Figure 3c–3e). The calculated CIE color coordinates can be used to characterize the emission spectra (Figure 7 and Supplementary Table S1). These values range from (0.162, 0.062) at $x = 0$ to (0.327, 0.361) at $x = 0.5$. The color tones are in accordance with the results of the fluorescence microscopy PL images.

In addition, the FWHM of the PL spectra was quite broad for samples $x \geqslant 0.3$ and covers a wide range of the visible spectrum. This is helpful for creating high CRI phosphor-converted WLEDs. For example, the composition at $x = 0.5$ can achieve greater CRI white-light versus commercial YAG:Ce³⁺-based WLEDs. This will be shown and discussed in Figure 8. A continuous redshift is also observed in the two emission bands with an increase in the B³⁺ content (see Supplementary Table S1). In our case, there are two possible causes for the PL redshift: (1) reabsorption; and (2) increased crystal field splitting of Eu²⁺. In reabsorption, the greater energy emission generally resonates with the lower energy part of the excitation spectra. This results in the partial reabsorption of the high-energy emission and a shift in the emission to the red. Herein, it is clear that the higher-energy emission overlaps the low energy PLE spectra (λ_{em} = 550 nm). The extent of the overlap becomes more prominent with an increase in the B³⁺ content. In the case of increased Eu²⁺ crystal fields, the lowest 5d energy level of Eu²⁺ is strongly influenced by the crystal field splitting. Therefore, the PL spectrum will redshift when the splitting of the Eu²⁺ 5d energy levels increases. As shown in the XRD section, the anionic polyhedron PO₄ units are successively replaced with BO₃ by increasing the B³⁺ content. This reduces the unit cell volume and decreases the Sr-O (Eu-O) bond length. A decreased Eu-O bond length possibly increases the crystal field splitting of the Eu²⁺ ions in the 5d energy level. This causes a continuous redshift in the emission spectra.

To validate this hypothesis, the EPR data were used to investigate the surroundings of the Eu²⁺ ions because the EPR signals from the Eu²⁺ ions are very sensitive to the area surrounding the Eu²⁺ ions (4f⁷, S = 7/2, L = 0). Figure 4 shows the EPR spectra of end member SPO_Cl and SPBO_Cl:0.04Eu²⁺ powders ($x = 0$, 0.2, 0.4, and 0.5), respectively. At $x = 0$, there is a very weak EPR signal for the SPO_Cl end member (no Eu) indicating that paramagnetic impurities exist in the host. These impurities may originate from sample defects. The weak EPR signal corresponding to the defects can be neglected compared with the EPR signal of the
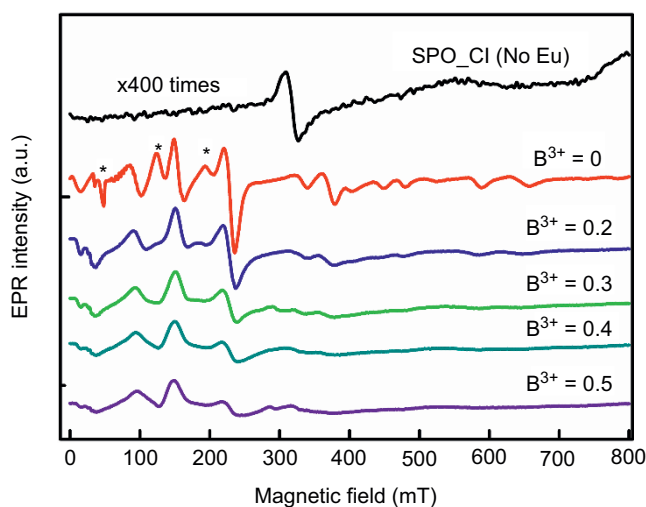

Figure 4 EPR spectra of the end member Sr₅(PO₄)₃Cl (SPO_Cl) and SPBO_Cl:0.04Eu²⁺.

SPO_Cl:0.04Eu²⁺. Accordingly, the EPR signals of the SPO_Cl:0.04Eu²⁺ can be totally attributed to the unpaired electrons in the Eu²⁺. We consider that the local coordination environments of Eu²⁺ can be divided into two sections: with and without B⁵⁺ ($x = 0$ and $x = 0.2$–0.5, respectively). These sections yield different emissions, including Eu(1) at 446 nm and Eu(2) at 550 nm. In contrast, the difference in the EPR signals (indicated by *) is likely due to changes in the Eu²⁺ sites in the host lattice with the addition of B⁵⁺. This result indicates that the introduction of B⁵⁺ induces a distinct Eu²⁺ site that may occupy the perturbed Sr site in the host lattice. Similar results have also been reported in the literature.[35] By increasing B⁵⁺ content, we found that the FWHM of the EPR spectra of SPBO_Cl:0.04Eu²⁺ ($x = 0.2$, 0.4, and 0.5) is gradually broadened. This result presents evidence that the introduction of B³⁺ significantly intensifies the interaction between Eu²⁺ centers and the host lattice[36], leading to an increase in the energy-level splitting of Eu²⁺ 5d. This redshifts the PL spectra. In addition, the Stokes shift for both emission bands changes with an increase in the B³⁺ content, but this change is not significant (see Supplementary Table S1). Therefore, we consider the redshift of the PL spectra to be primarily due to reabsorption and increased crystal filed splitting of Eu²⁺. Of course, the contribution of the Stokes shift to the observed redshift cannot be ruled out.

The normalized PLE spectra for Sr₅(PO₄)₃₋ₓ(BO₃)ₓCl:0.04Eu²⁺ ($x = 0$, 0.1, 0.2, 0.3, 0.4, and 0.5) samples were obtained using the maxima value of each PL band. Monitoring the blue emission showed that the PLE spectrum has a broad band from 250 nm to 440 nm (Figure 5a). Similarly, when monitoring yellow emission, broad PLE spectra were observed in the range of 250–475 nm (Figure 5b). Both PLE spectra are ascribed to the 4f→5d transitions of Eu²⁺. Nevertheless, different spectral profiles for the two PLE bands suggest that there is a difference in the splitting of the 4f⁶5d¹ excited states for the two sites. This concurs with the PL and EPR results.

When increasing the B³⁺ content, the Eu²⁺ 5d bands in both PLE spectra shift to the lower-energy side along with profile changes. This is a consequence of the stronger crystal field splitting of the Eu²⁺ ions' 5d energy level as discussed previously. In addition, the bandgaps (E_g) of SPO_Cl, SPBO_Cl, and SPBO_Cl:0.04Eu²⁺ are calculated from their reflectance spectra. The undoped sample shows no absorption in the wavelength range greater than 375 nm and is thus white, which agrees with the PLE results. The E_g of SPO_Cl is estimated to be 3.836 eV. The SPBO_Cl:0.04Eu²⁺ has a strong absorption from 250 nm to 475 nm, and the color turns light yellow (see Supplementary Figure S3). This result is attributed to the 4f–5d transitions at the Eu²⁺ center. The E_g of SPBO_Cl:0.04Eu²⁺ is estimated to be 2.850 eV. The PL spectra (λ_{ex} = 365 nm) of SPO_Cl:0.04Eu²⁺ is also shown in Figure 5b as a reference. Obviously, there is a significant spectral overlap between the blue emission located at 446 nm (Eu(1)) and the PLE spectra monitored by the lower-energy emissions of Eu(2) from 410 nm to 470 nm. This result implies the possibility of energy transfer from the Eu(1) to the Eu(2) site.

To further investigate the dynamic luminescence process between the higher-energy emission sites and the lower-energy emission sites, the lifetime decay of the higher-energy emission sites in the SPBO_Cl:0.04Eu²⁺ powders ($x = 0$, 0.1, 0.3, and 0.5) was recorded (λ_{ex} = 365 nm; Figure 6a). At $x = 0$, the decay curve of the higher-energy emission at 446 nm presents a single exponential decay behavior. However, the fluorescence decay of the higher-energy emission becomes faster with an increase in the B³⁺ content, and the decay curves are non-exponential. This suggests that the incorporation of B⁵⁺ ions changes the luminescence dynamic process of Eu²⁺. The average lifetime (τ) of these samples can be estimated using Equation (1)[37]:
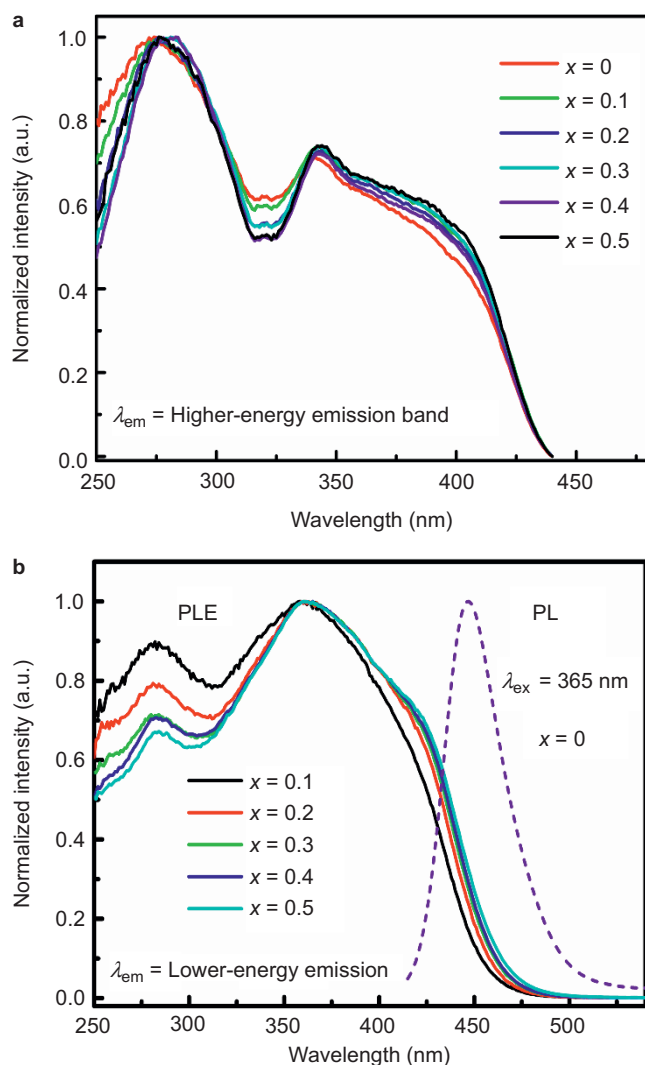
Figure 5 (**a**) Normalized PLE spectra of the SPBO_Cl:0.04Eu²⁺ (0 ⩽ *x* ⩽ 0.5) obtained by monitoring the higher-energy emission. (**b**) Normalized PLE spectra of the SPBO_Cl:0.04Eu²⁺ (0 ⩽ *x* ⩽ 0.5) obtained by monitoring the lower-energy emission. Additionally, the PL spectrum of $Sr_5(PO_4)_3Cl:0.04Eu^{2+}$ is also shown as a reference.

$$\tau = \frac{\int_0^\infty I(t)t\,dt}{\int_0^\infty I(t)\,dt} \tag{1}$$

where $I(t)$ is the luminous intensity at time t. According to Equation (1), the average lifetimes of higher-energy emission are 0.56, 0.47, 0.39, and 0.32 μs for B³⁺ values of 0, 0.1, 0.3, and 0.5, respectively. The decrease in the lifetime of the higher-energy emission with an increase in the B³⁺ content strongly demonstrates an energy transfer from the higher-energy emission sites to the lower-energy emission sites. In this case, the calculated lifetime values corresponding to the higher-energy emission cannot be completely assigned to the 446-nm Eu(1) sites because the 446- and 462-nm emissions from the Eu(1) site are simultaneously recorded (Supplementary Fig. S1). With regard to the lifetime of the Eu(2) acceptor, an initial increasing trend should be observed if the energy transfer from the higher-energy emission to the lower-energy emission sites definitely occurs. Figure 6b shows the decay profile of the lower-energy emission (λ_{em} = 550 nm) for *x* = 0.1 samples at an excitation of
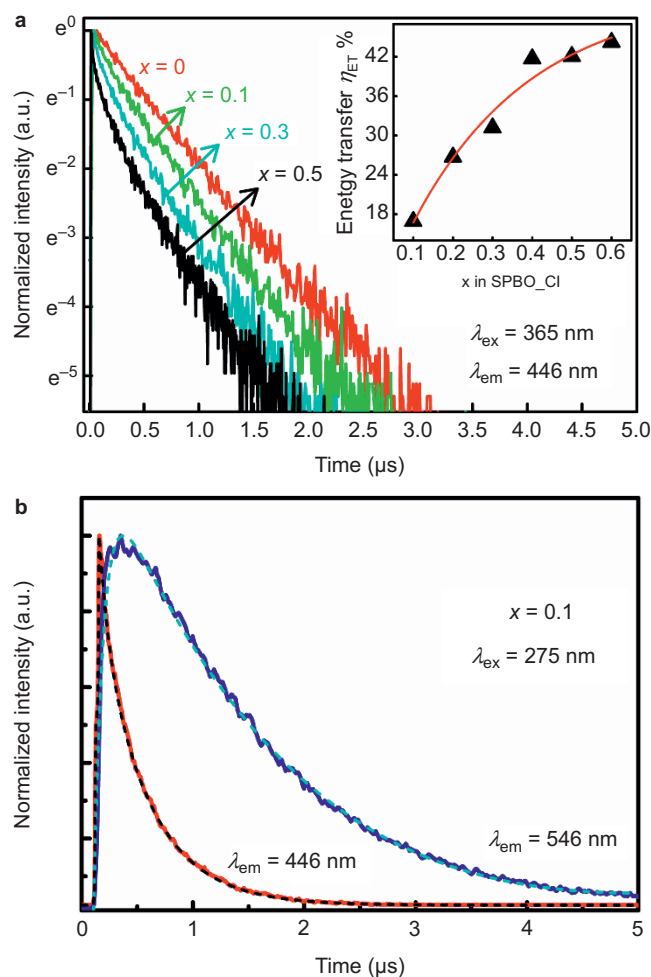

Figure 6 (**a**) The lifetime decay curves for the Eu(1) in SPBO_Cl:0.04Eu²⁺ phosphors (*x* = 0, 0.1, 0.3, and 0.5) excited at 365 nm and monitored at 446 nm. The inset shows the calculated energy transfer efficiency (η_{ET}) from Eu(1) to Eu(2) with a varying B³⁺ doping content. (**b**) The lifetime decay curves for Eu²⁺ in the SPBO_Cl:0.04Eu²⁺ (*x* = 0.1) phosphor excited at 275 nm and monitored at 448 and 564 nm. The lifetime decay curves were fitted using the double-exponential equation $I(t) = I_0 + A_1\exp(-t/\tau_1) + A_2\exp(-t/\tau_2)$.

275 nm. This clearly shows that the decay profile is nonexponential with a prominent initial increasing trend. The calculated average lifetime using Equation (1) is 1.44 μs with a buildup characterized by a constant ~0.37 μs. In contrast, the decay monitored the higher-energy emission (λ_{em} = 446 nm) is multi-exponential with the fastest component at ~0.38 μs. The similarity in this time constant for the fastest decay component of the higher-energy emission as well as the increase in the lower-energy emission also suggests the occurrence of energy transfer from the higher-energy emission sites to the lower-energy emission sites.

The different decay profiles and lifetime values for the blue and yellow emissions further support the notion of the two emission bands from two distinct Eu²⁺ centers. In addition, the energy transfer efficiency (η) from the higher-energy emission to the lower-energy emission sites can be estimated using Equation (2)[38,39]:

$$\eta = 1 - \tau_s/\tau_{so} \tag{2}$$

where τ_{so} and τ_s are the lifetimes of the higher-energy emission sites in the absence and in the presence of the lower-energy emissions, respectively. As shown in the inset of Figure 6b, η increases gradually with an
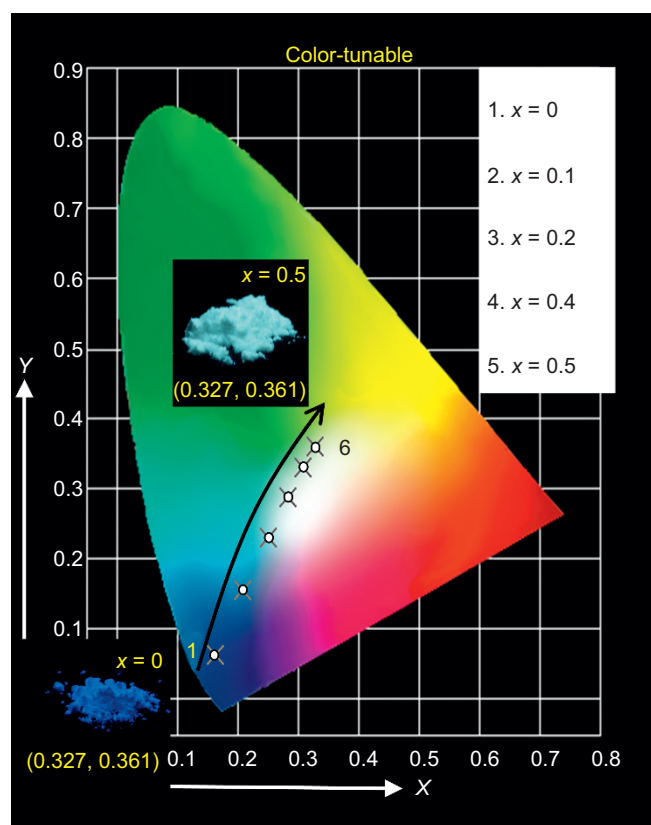
Figure 7 The CIE chromaticity coordinates the SPBO_Cl:0.04Eu²⁺ phosphors ($x = 0$, 0.1, 0.2, 0.4, and 0.5) under excitation at 365 nm.

Figure 8 The PL spectrum of $Sr_5(PO_4)_{2.5}(BO_3)_{0.5}Cl:0.04Eu^{2+}$ phosphor under excitation at 365 nm (red line). The electroluminescence spectrum of the commercial YAG:Ce³⁺-based WLED driven by forward-bias current at 20 mA is also plotted as a reference.

increase in the B³⁺ content. More precisely, the energy-transfer efficiencies, η, are calculated to be 0%, 16.9%, 26.7%, 31.2%, 41.7%, 42.1%, and 44.2% for SPBO_Cl:0.04Eu²⁺ when $x = 0$, 0.1, 0.2, 0.3, 0.4, 0.5, and 0.6, respectively.

To evaluate the potential application of an as-prepared sample, the PL spectrum of the SPBO_Cl:0.04Eu²⁺ phosphor ($x = 0.5$) at a 365-nm excitation is recorded and presented in Figure 8. White light can clearly be generated by combining the blue emission located at approximately 455 and the yellow emission at 550 nm. Interestingly, the white-light emission profile of the as-prepared sample is very similar to the emission profile of the commercial WLED (blue LED chip + $Y_3Al_5O_{12}:Ce^{3+}$ (YAG:Ce³⁺) yellow-emitting phosphor).

For comparison, the EL spectrum of the commercial WLED driven by a forward bias at 20 mA is also presented in Figure 8. The full set of 8 CRIs and the average CRI (Ra) of the as-prepared sample as well as the commercial WLEDs are listed in Supplementary Table S2, respectively. All 8 CRIs are greater than the YAG:Ce³⁺-based WLED. The as-prepared sample has a greater Ra value (~91.0) versus the YAG:Ce³⁺-based WLED (~80.2). Ra is widely used in the lighting community to evaluate the performance of artificial lighting including WLEDs[40–42]; however, a high Ra does not completely guarantee the good saturation of colors of illuminated objects[43] because the Ra is calculated only using the first eight (R1–R8) values of the CIE from the recommended 14 test color samples[43]. Therefore, the special CRI R9 value, which denotes the color reproduction in the strong red region and is very important for biomedical and painting[44–48], is critical for high-quality color renditions of the light source. Therefore, we found that the R9 of the as-prepared sample is greater (~90.2) than the R9 of the current available lamp sources,
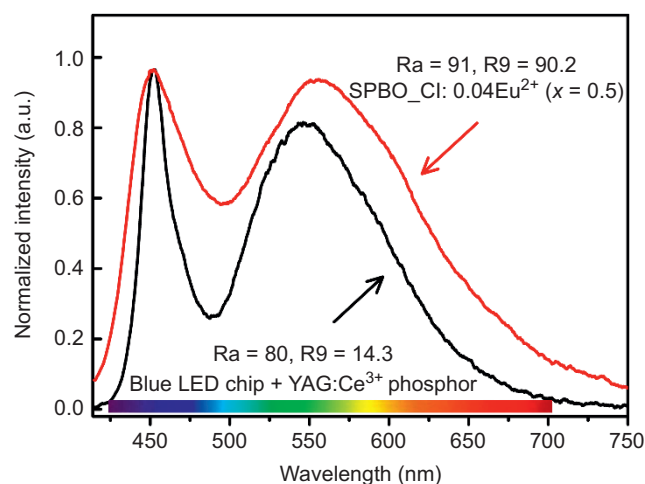
e.g., halo-fluorescent lamps (~–81)[47], tri-phosphor fluorescent lamps (~8)[47], and commercial WLEDs (~14.3) (see Supplementary Table S3). Compared with the YAG:Ce³⁺-based commercial WLED, the as-prepared sample has greater Ra and R9 values. This is consistent with the fact that there was greater number of blue-greenish (470–515 nm) and deep-red components in the emission spectrum and a wider spectral distribution (~137 nm) at approximately 550 nm compared with the YAG:Ce³⁺ phosphor (~104 nm).

Thus far, there have been many investigations of single Eu²⁺/Ce³⁺-activated white-light phosphors, e.g., $(BaSrMg)(PO_4)_2:Eu^{2+}$ (Ra = 87)[19], $(Na_{1-x}Ca_x)(Sc_{1-x}Mg_x)Si_2O_6:Eu^{2+}$ (Ra = 72)[20], $(Gd_{1-x}Sr_{2+x})AlO_{5-x}F_x:Eu^{2+}$ (Ra = 53)[21], $Sr_2Ba(AlO_4F)_{1-x}(SiO_5)_x:Ce^{2+}$ (Ra = 70)[22], $(La_{0.075-x}Ce_{0.025}Sr_{2+x})(Al_{1-x}Si_xO_5)$ (Ra = 70)[23], and $(Sr_{2.975}Ce_{0.025})Al_{1-x}Si_xO_{4+x}F_{1-x}$ (Ra = 69)[24]. However, indices greater than Ra = 91.0 and R9 = 90.2 have not yet been reported. These results indicate that this single-phased SPBO_Cl:0.04Eu²⁺ white-light phosphor is a promising candidate for NUVLED-excited devices for general illumination purposes.

Thermal stability is an important technological parameters for a WLED phosphor. The thermal quenching behavior of the SPBO_Cl:0.04Eu²⁺ phosphor ($x = 0.5$) in the temperature range of 20–200 °C under an excitation at 365 nm is shown in Supplementary Fig. S4. The emission intensity of Eu²⁺ decreased with an elevated temperature (Supplementary Fig. S4a). The emission intensity decreased to 50% of the initial values at 120 °C (Supplementary Fig. S4b). Furthermore, the thermal quenching temperatures for both emission bands of the SPBO_Cl:0.04Eu²⁺ phosphor were different (Supplementary Fig. S4c). The thermal quenching temperature for the yellow emission was 150 °C, whereas that for blue was 90 °C. Different thermal quenching temperatures for the blue and the yellow emissions may originate from the distinct Eu²⁺ ions with different rigid environments. As for the solid-solution white-light phosphor ($x = 0.5$), the thermally activated energy was calculated in terms of the Arrhenius equation $I(T) \approx I_0[1 + A \exp(-\Delta E/k_B T)]^{-1}$ (where I_0 is the initial intensity, $I(T)$ is the intensity at a given temperature T, A is a constant, ΔE is the activation energy for the thermal quenching, and k_B is Boltzmann's constant). The large decrease in luminescence might be attributed to the smaller barrier energy (~0.269 eV).

CONCLUSIONS

The $Sr_5(PO_4)_{3-x}(BO_3)_xCl:0.04Eu^{2+}$ phosphors demonstrate a continuously tunable emission and were obtained using a solid-solution method and a solid-state reaction. Based on the Rietveld and EPR analysis, substituting PO_4 with BO_3 anionic polyhedrons contracts and distorts the lattice of the end member $Sr_5(PO_4)_3Cl$ of the solid solution. This induces a new Eu^{2+} yellow emission at approximately 550 nm. The distinct Eu^{2+} center originates from the Eu^{2+}, occupying a different crystal field site. Combining a blue emission near 446 nm and an induced yellow emission at 550 nm results in a tunable emission including white light via 365-nm excitation. Significantly, the white-light phosphor presents greater Ra and R9 values (91 and 90.2, respectively) relative to commercial YAG:Ce^{3+}-based WLEDs (Ra = 80 and R9 = 14.3). This study provides an important shortcut for developing a high CRI white-light phosphor from single-Eu^{2+}-doped compounds.

1   Yamamoto H. White LED phosphors: the next step. In: Jiang SB, Digonnet MJF, Glesener JW, Dries JC, editors. *Proceedings of SPIE optical components and materials VII; 23 January 2010*, Vol. 7598. San Francisco, CA: SPIE; 2010. pp 759808–759811.

2   Hartmann P, Pachler P, Payrer EL, Tasch S. Up and down: color conversion for solid-state lighting. In: Streubel KP, Jeon H, Tu LW, editors. *Proceedings of SPIE light-emitting diodes: materials, devices, and applications for solid state lighting XIII; 24 January 2009*, Vol. 7231. San Jose, CA: SPIE; 2009. p 72310X.

3   Li XF, Budai JD, Liu F, Howe JY, Zhang JH *et al.* New yellow Ba$_{0.93}$Eu$_{0.07}$Al$_2$O$_4$ phosphor for warm-white light-emitting diodes through single-emitting-center conversion. *Light Sci Appl* 2013; **2**: e50; doi:10.1038/lsa.2013.6.

4   Shang MM, Li CX, Lin J. How to produce white light in a single-phase host? *Chem Soc Rev* 2014; **43**: 1372–1386.

5   Hao ZD, Zhang JH, Zhang X, Sun XY, Luo YS *et al.* White light emitting diode by using α-Ca$_2$P$_2$O$_7$:Eu^{2+}, Mn^{2+} phosphor. *Appl Phys Lett* 2007; **90**: 261113.

6   Chang CK, Chen TM. White light generation under violet-blue excitation from tunable green-to-red emitting Ca$_2$MgSi$_2$O$_7$: Eu, Mn through energy transfer. *Appl Phys Lett* 2007; **90**: 161901.

7   Wu WW, Xia ZG. Synthesis and color-tunable luminescence properties of Eu^{2+} and Mn^{2+}-activated Ca$_3$Mg$_3$(PO$_4$)$_4$ phosphor for solid state lighting. *RSC Adv* 2013; **3**: 6051–6057.

8   Chen X, Dai PP, Zhang XT, Li C, Lu S *et al.* A highly efficient white light (Sr$_3$, Ca, Ba)(PO$_4$)$_3$Cl:Eu^{2+}, Tb^{3+}, Mn^{2+} phosphor via dual energy transfers for white light-emitting diodes. *Inorg Chem* 2014; **53**: 3441–3448.

9   Lü W, Hao ZD, Zhang X, Luo YS, Wang XJ *et al.* Tunable full-color emitting BaMg$_2$Al$_6$Si$_9$O$_{30}$: Eu^{2+}, Tb^{3+}, Mn^{2+} phosphors based on energy transfer. *Inorg Chem* 2011; **50**: 7846–7851.

10 Geng DL, Shang MM, Yang DM, Zhang Y, Cheng ZY *et al.* Green/green-yellow-emitting KSrGd(PO$_4$)$_2$: Ce^{3+}, Tb^{3+}/Mn^{2+} phosphors with high quantum efficiency for LEDs and FEDs. *Dalton Trans* 2012; **41**: 14042–14045.

11 Jiao MM, Jia YC, Lü W, Lv WZ, Zhao Q *et al.* A single-phase white-emitting Ca$_2$SrAl$_2$O$_6$:Ce^{3+}, Li$^+$, Mn^{2+} phosphor with energy transfer for UV-excited WLEDs. *Dalton Trans* 2014; **43**: 3202–3209.

12 Li GG, Geng DL, Shang MM, Zhang Y, Peng C *et al.* Color tuning luminescence of Ce^{3+}/Mn^{2+}/Tb^{3+}-triactivated Mg$_2$Y$_8$(SiO$_4$)$_6$O$_2$ via energy transfer: potential single-phase white-light-emitting phosphors. *J Phys Chem C* 2011; **115**: 21882–21892.

13 Huang CH, Chen TM. A novel single-composition trichromatic white-light Ca$_3$Y (GaO)$_3$(BO$_3$)$_4$:Ce^{3+}, Mn^{2+}, Tb^{3+} phosphor for UV-light emitting diodes. *J Phys Chem C* 2011; **115**: 2349–2355.

14 Li GG, Zhang Y, Geng DL, Shang MM, Peng C *et al.* Single-composition trichromatic white-emitting Ca$_4$Y$_6$(SiO$_4$)$_6$O: Ce^{3+}/Mn^{2+}/Tb^{3+} phosphor: luminescence and energy transfer. *ACS Appl Mater Interfaces* 2012; **4**: 296–305.

15 Setlur AA, Shiang JJ, Happek U. Eu^{2+}–Mn^{2+} phosphor saturation in 5 mm light emitting diode lamps. *Appl Phys Lett* 2008; **92**: 081104.

16 Happek U, Setlur AA, Shang JJ. Inverse bottleneck in Eu^{2+}–Mn^{2+} energy transfer. *J Lumin* 2009; **129**: 1459–1463.

17 Yang FL, An W, Zhuang WD, Tian GS, Jing XP. Energy transfer from Eu^{2+} to Mn^{2+} in M$_5$(PO$_4$)$_3$Cl (M = Ca, Sr). *J Lumin* 2014; **146**: 269–274.

18 Yang FL, An W, Wei HW, Chen GT, Zhuang WD *et al.* Comparison of the PL properties of Eu^{2+}, Mn^{2+} co-doped M$_5$(PO$_4$)$_3$Cl (M = Ca, Sr, Ba). *J Alloys Compd* 2014; **590**: 535–540.

19 Wu ZC, Liu J, Hou WG, Xua J, Gong ML. A new single-host white-light-emitting BaSrMg (PO$_4$)$_2$:Eu^{2+} phosphor for white-light-emitting diodes. *J Alloys Compd* 2010; **498**: 139–142.

20 Xia ZG, Zhang YY, Molokeev MS, Atuchin VV, Luo Y. Linear structural evolution induced tunable photoluminescence in clinopyroxene solid-solution phosphors. *Sci Rep* 2013; **3**: 3310.

21 Im WB, Fourré Y, Brinkley S, Sonoda J, Nakamura SJ *et al.* Substitution of oxygen by fluorine in the GdSr$_2$AlO$_5$:Ce^{3+} phosphors: Gd$_{1-x}$Sr$_{2+x}$AlO$_{5-x}$Fx solid-solutions for solid state white lighting. *Opt Express* 2009; **17**: 22673–22679.

22 Denault KA, Georege NC, Paden SR, Brinkley S, Mikhailovsky AA *et al.* A green-yellow emitting oxyfluoride solid-solution phosphor Sr$_2$Ba(AlO$_4$F)$_{1-x}$(SiO$_5$)$_x$:Ce^{3+} for thermally stable, high color rendition solid state white lighting. *J Mater Chem* 2012; **22**: 18204–18213.

23 Im WB, Fellows NN, DenBaars SP, Seshadri R. La$_{1-x-0.025}$Ce$_{0.025}$Sr$_{2+x}$Al$_{1-x}$Si$_x$O$_5$ solid solutions as tunable yellow phosphors for solid state white lighting. *J Mater Chem* 2009; **19**: 1325–1330.

24 Im WB, George N, Kurzman J, Brinkley S, Mikhailovsky A *et al.* Efficient and color-tunable oxyfluoride solid solution phosphors for solid-state white lighting. *Adv Mater* 2011; **23**: 2300–2305.

25 Bachmann V, Ronda C, Oeckler O, Schnick WG, Meijerink A. Color point tuning for (Sr, Ca, Ba)Si$_2$O$_2$N$_2$:Eu^{2+} for white light LEDs. *Chem Mater* 2009; **21**: 316–325.

26 Song YH, You HP, Yang M, Zheng YH, Liu K *et al.* Facile synthesis and luminescence of Sr$_5$(PO$_4$)$_3$Cl:Eu^{2+} nanorod bundles via a hydrothermal route. *Inorg Chem* 2010; **49**: 1674–1678.

27 Guo C, Luan L, Ding X, Zhang F, Shi FG *et al.* Luminescent properties of Sr$_5$(PO$_4$)$_3$Cl: Eu^{2+}, Mn^{2+} as a potential phosphor for UV-LED based white LEDs. *Appl Phys B* 2009; **95**: 779–785.

28 Zeng Q, Liang HB, Zhang GB, Birowosuto MD, Tian ZF *et al.* Luminescence of Ce^{3+} activated fluoro-apatites M$_5$(PO$_4$)$_3$F (M = Ca, Sr, Ba) under VUV–UV and x-ray excitation. *J Phys Condens Matter* 2006; **18**: 9549–9560.

29 Gruber JB, Zandi B, Merkle L. Crystal-field splitting of energy levels of rare-earth ions Dy^{3+}4f^9 and Yb^{3+}, 4f^{13} in M(II) sites in the fluorapatite crystal Sr$_5$(PO$_4$)$_3$F. *J Appl Phys* 1998; **83**: 1009–1017.

30 Alekel T, Keszler DA. Structure of Sr$_5$(BO$_3$)$_3$Cl. *Acta Cryst C* 1992; **48**: 1382–1386.

31 Zhang QH, Wang J, Yu RJ, Zhang M, Su Q. Luminescence properties of Eu^{2+} ions in Sr$_5$(BO$_3$)$_3$Cl. *Electrochem Solid-State Lett* 2008; **11**: H335–H337.

32 Larson AC, Von Dreele RB. *General structure analysis system (GSAS)*. Report LAUR 86-748; Los Alamos National Laboratory, University of California, Los Alamos, NM; 2004.

33 Nagpure IM, Pitale SS, Coetsee E, Ntwaeaborwa OM, Terblans JJ *et al.* Lattice site dependent cathodoluminescence behavior and surface chemical changes in a Sr$_5$(PO$_4$)$_3$F host. *Phys B* 2012; **407**: 1505–1508.

34 McKittrick J, Hannah ME, Piquette A, Han JK, Choi JI *et al.* Phosphor selection considerations for near-UV LED solid state lighting. *ECS J Solid State Sci Technol* 2013; **2**: R3119–R3131.

35 Im WB, Kim YI, Yoo HS, Jeon DY. Luminescent and structural properties of (Sr$_{1-x}$, Ba$_x$)$_3$MgSi$_2$O$_8$:Eu^{2+}: effects of Ba content on the Eu^{2+} site preference for thermal stability. *Inorg Chem* 2009; **48**: 557–564.

36 Xu YZ. *Applied electron magnetic resonance spectroscopy*. Beijing: Science Press; 2008. pp 163–164.

37 Guo N, Song YH, You HP, Jia G, Yang M *et al.* Optical properties and energy transfer of NaCaPO$_4$:Ce^{3+}, Tb^{3+} phosphors for potential application in light-emitting diodes. *Eur J Inorg Chem* 2010; **29**: 4636–4642.

38 Lahoz F, Martín IR, Méndez-Ramos J, Núñez P. Dopant distribution in a Tm^{3+}-Yb^{3+} codoped silica based glass ceramic: an infrared-laser induced upconversion study. *J Chem Phys* 2004; **120**: 6180–6190.

39 Paulose PI, Jose G, Thomas V, Unnikrishnan NV, Warrier MKR. Sensitized fluorescence of Ce^{3+}/Mn^{2+} system in phosphate glass. *J Phys Chem Solids* 2003; **64**: 841–846.

40 Huang CH, Chen TM. Novel yellow-emitting Sr$_8$MgLn(PO$_4$)$_7$:Eu^{2+} (Ln = Y, La) phosphors for applications in white LEDs with excellent color rendering index. *Inorg Chem* 2011; **50**: 5725–5730.

41 Jang HS, Yang HS, Kim SW, Han JY, Lee SG *et al.* White light-emitting diodes with excellent color rendering based on organically capped CdSe quantum dots and Sr$_3$SiO$_5$:Ce^{3+} phosphors. *Adv Mater* 2008; **20**: 2696–2702.

42 Kimura N, Sakuma K, Hirafune S, Asano K, Hirosaki N *et al.* Extra high color rendering white light-emitting diode lamps using oxynitride and nitride phosphors excited by blue light-emitting diode. *Appl Phys Lett* 2007; **90**: 051109.

43 Oh JH, Yang SJ, Do YR. Healthy, natural, efficient and tunable lighting: four-package white LEDs for optimizing the circadian effect, color quality and vision performance. *Light Sci Appl* 2014; **3**: e141; doi:10.1038/lsa.2014.22.

44 Kwon KH, Im WB, Jang HS, Yoo HS, Jeon DY. Luminescence properties and energy transfer of site-sensitive Ca$_{6-x-y}$Mg$_{x-z}$(PO$_4$)$_4$:Eu$_y^{2+}$, Mn$_z^{2+}$ phosphors and their application to near-UV LED-based white LEDs. *Inorg Chem* 2009; **48**: 11525–11532.

45 Wang XB, Yan XS, Li WW, Sun K. Doped quantum dots for white-light-emitting diodes without reabsorption of multiphase phosphors. *Adv Mater* 2012; **24**: 2742–2747.

46 Fukui T, Kamon K, Takeshita J, Hayashi H, Miyachi T *et al*. Superior illuminant characteristics of color rendering and luminous efficacy in multilayered phosphor conversion white light sources excited by near-ultraviolet light-emitting diodes. *Jpn J Appl Phys* 2009; **48**: 112101.
47 Narukawa Y, Ichikawa M, Sanga D, Sano M, Mukai T. White light emitting diodes with super-high luminous efficacy. *J Phys D Appl Phys* 2010; **43**: 354002.
48 Narukawa Y, Narita J, Sakamoto T, Yamada T, Narimatsu H *et al*. Recent progress of high efficiency white LEDs. *Phys Status Solidi A* 2007; **204**: 2087–2093.

Supplementary information for this article can be found on the *Light: Science & Applications*' website (http://www.nature.com/lsa/).